

Spectator-transition crosstalk in a spin-3/2 silicon-vacancy qudit in silicon carbide revealed by broadband Ramsey interferometry

Jun-Jae Choi,^{1,†} Seung-Jae Hwang,^{1,†} Seoyoung Paik,¹ Juhwan Kim,² Jawad UI-Hassan,³ Nguyen Tien Son,³ Hiroshi Abe,⁴ Takeshi Oshima,^{4,5} Jaekwon Suk,⁶ Hyeyon-Ho Jeong,² Dong-Hee Kim,¹ Sang-Yun Lee^{1,*}

¹ Department of Physics and Photon science, Gwangju Institute of Science and Technology, Cheomdan-gwagiro 123, Gwangju, Republic of Korea

² Department of Electrical Engineering & Computer Science, Gwangju Institute of Science and Technology, Cheomdan-gwagiro 123, Gwangju, Republic of Korea

³ Department of Physics, Chemistry and Biology, Linköping University, SE-581 83 Linköping, Sweden

⁴ National Institutes for Quantum Science and Technology (QST), Takasaki, Gunma 370-1292, Japan

⁵ Department of Materials Science, Tohoku University, Sendai, Miyagi 980-8579, Japan

⁶ Korea Multi-purpose Accelerator Complex, Korea Atomic Energy Research Institute, Gyeongju, 38180, Republic of Korea

Color-center spins in 4H-SiC offer a rare combination of wafer-scale materials maturity with long spin coherence and chip-level photonics, making them promising building blocks for scalable quantum technologies. In particular, the silicon vacancy hosts an $S = 3/2$ ground state, a native qudit that enables compact encodings and subspace-selective control, but also introduces spectator transitions: short, detuned pulses can coherently drive non-addressed level pairs and create crosstalk. Here we use broadband Ramsey interferometry to reveal and quantify such spectator-transition crosstalk. Experimentally, the Ramsey Fourier spectra display multiple lines beyond the addressed single quantum transition. Analytically, we map each line to a pairwise energy difference between qudit levels of the rotating-frame Hamiltonian and assign its weight via compact amplitudes set by the prepared state and the microwave pulse parameters, predicting a deterministic six-branch structure. Numerical time-domain propagation with the experimental sampling reproduces the detuning map, and the measured peak positions coincide with the analytic branch lines without frequency fitting. Together these results provide a practical, spectator-aware framework for multilevel control in the silicon-vacancy qudit. The approach offers clear guidance to suppress crosstalk or, conversely, to exploit spectator lines for example as additional constraints for in-situ pulse calibration and for phase-sensitive quantum state/process estimation.

[†] These authors contributed equally

* sangyunlee@gist.ac.kr

I. INTRODUCTION.

Color-centers in 4H-SiC have rapidly matured into a semiconductor platform for quantum technologies. Leading contenders such as the silicon vacancy and the divacancy combine long-lived, optically addressable spins with high-quality nanophotonics, bringing high-fidelity spin–photon interfaces within practical reach and, by extension, quantum-repeater and network architectures [1,2]. Recent milestones highlight device-level control of essential quantum properties of these centers: standard optoelectronic structures, e.g., Schottky and PIN junctions, can tune the local charge environment and Stark-shift single defects, narrowing zero-phonon lines toward the lifetime-limit required for generating indistinguishable photons in Hong–Ou–Mandel Bell-state measurements, as well as enhancing spin coherence [3-5]. In parallel, nanophotonic waveguides and cavities preserve lifetime-limited optical transitions and robust spin control, including coherent manipulation of nearby nuclear registers [2]. Thin-film SiC-on-insulator studies have chiefly showcased photonic integration and on-chip frequency conversion [6]. While these advances have been driven by various color centers, the negatively charged silicon vacancy stands out because its optical transition dipole has a single orientation aligned with the crystal c-axis [7,8], which simplifies deterministic coupling to nanophotonic modes, and its spin quantization axis is also along the c-axis for all sites [9,10], that supports scalable multi-spin registers and higher multi-qubit gate fidelities. Also, its optical lines remain close to the lifetime-limit after nanofabrication and up to 20 K [2,11].

A distinctive feature of the negatively charged silicon vacancy in 4H-SiC is its spin-3/2 ground state [12,13], which realizes a natural four-level qudit, i.e., a ququart [14]. Such multilevel structure can support higher information density per physical carrier [15] and reduced circuit depth in some architectures [16,17], hardware-efficient quantum error correction [18], and multi-transition sensing in time-domain interferometry [19]. At the same time, closely spaced transitions make the system susceptible to off-resonant driving: bandwidth-broad microwave pulses can unintentionally excite spectator transitions, non-addressed transitions that acquire coherence under off-resonant coupling [20]. This produces coherent leakage, i.e., drive-induced population transfer outside the intended subspace [21], and cross-talk, i.e., unintended excitation or correlated errors mediated by residual couplings or control spillover [22]. These considerations are not unique to any single platform since most physical platforms used for quantum information, including superconducting circuits [23], trapped ions and neutral atoms

[24,25], and defect spins [26], are inherently multilevel even when treated as qubits. Reducing such systems to two levels simplifies control and modeling but can hide off-resonant excitation and state mixing that limit gate and readout fidelities [27], bias tomographic reconstruction [28], and complicate error characterization by introducing correlated, cross-talk-mediated errors [22]. Such effects grow with spin quantum number and with the use of spectrally broad, time-efficient pulses. These benefits and challenges motivate explicit modeling and experimental diagnosis of multilevel pathways of the silicon vacancy in 4H-SiC rather than qubit-only approximations.

Optically detected magnetic resonance (ODMR) provides the measurement backbone: continuous-wave ODMR maps transition frequencies and the zero-field splitting (ZFS), while pulsed ODMR enables time-domain protocols such as Rabi, Ramsey, and Hahn-echo. Among these, Ramsey interferometry is phase-sensitive to detuning and, with short hard $\frac{\pi}{2}$ pulses, its spectral bandwidth overlaps neighboring transitions, making it a sensitive probe of multilevel subspaces. In practice, Ramsey-type measurements are a workhorse for phase-sensitive state characterization, including estimation of detunings and coherences, and are routinely embedded in quantum state/process tomography (QST/QPT) workflows across multiple platforms [29-32]. In this work, we implement broadband Ramsey spectroscopy to probe multilevel dynamics in the 4H-SiC silicon-vacancy ququart, resolving crosstalk and coherent spectator excitation among the sublevels. In 4H-SiC, the two crystallographic variants of the negatively charged silicon vacancy, $V1$ (h-site) and $V2$ (k-site), exhibit different ground-state ZFS: $2D_{gs}/2\pi \approx 4.5$ MHz and 70 MHz for $V1$ and $V2$, respectively [12,13]. We therefore use the $V1$ center as a testbed whose small ZFS brings neighboring transitions within the bandwidth of short $\pi/2$ pulses, enhancing Ramsey's sensitivity to off-resonant pathways without large frequency excursions. Below we refer to such off-resonant, non-addressed sublevel pairs that nevertheless acquire coherence during the sequence as spectator transitions [20]. Using this choice, we show, via simulations supported by analytical modeling, that a resonant drive seeds coherent amplitudes in spectator transitions; during free precession the full four-level density matrix accumulates multiple relative phases across pairwise coherences, and the final $\pi/2$ pulse mixes a subset of these coherences into measurable population modulations, yielding detuning-dispersive, multi-frequency Ramsey spectra. We map how detuning and drive strength redistribute spectral weight among the $m_S = \pm 3/2, \pm 1/2$ components and provide an interpretive

framework for multi-frequency Ramsey spectra in spin 3/2 systems, linking the six detuning-dependent frequency components resolved in our spectra to specific pairwise coherences and their phase evolution. Looking ahead, a phase-resolved, multi-frequency view of Ramsey signals may help future efforts to better understand and exploit qudits for example by informing gate design and error budgets, supporting sensing strategies that leverage sublevel-dependent shifts, or, where appropriate, augmenting measurement sets in state or process estimation.

II. METHODS

A. Sample and experimental setup

The sample used in this study is a 28 μm thick 4H- $^{28}\text{Si}^{12}\text{C}$ silicon carbide layer grown by chemical vapor deposition on a n-type a-plane 4H-SiC wafer. The isotope purity of the epitaxially grown layer is $\sim 99.85\%$ for ^{28}Si and $\sim 99.98\%$ for ^{12}C as determined from secondary ion mass spectrometry for a representative wafer from the same growth series. The background doping concentration of the N shallow donor is in the range of $\sim 3 \times 10^{15} \text{ cm}^{-3}$. Prior to the silicon vacancy creation, the layer was annealed at 1150 $^{\circ}\text{C}$ for one hour to reduce surface defects. The isolated silicon vacancies were then introduced by electron irradiation. The sample was irradiated with 2 MeV electrons at a fluence of $1 \times 10^{12} \text{ cm}^{-2}$ with a flux of $4.8 \times 10^{10} \text{ cm}^{-2} \text{ s}^{-1}$ at room temperature yielding a low density of well-isolated silicon vacancies, approximately one V1 center per $1 \mu\text{m}^2$ (estimated from confocal fluorescence scans). After irradiation, the sample was annealed at 400 $^{\circ}\text{C}$ for 30 min to remove some interstitial-related defects. In addition, 200 keV proton irradiation with a fluence of $1 \times 10^{15} \text{ cm}^{-2}$ was performed through a 60 μm thick aluminum mask to create an ensemble of silicon vacancies near one edge of the sample; this ensemble was used as a bright ensemble reference for the magnetic field alignment [9,33].

The experiments were performed in a cryogenic confocal microscope. A closed-cycle cryostat (Montana Instruments s200) was used to cool the sample to $\sim 4\text{-}5 \text{ K}$. Inside the cryostat, a three-axis low-temperature nanopositioning stage was employed to scan the sample. We used a Zeiss EC Epiplan-Neofluar 100 \times , NA 0.75 air objective, with the excitation beam incident horizontally onto the sample. A 785 nm laser (Thorlabs L785H1) was used for depolarization of the ground state spin-sublevels and an 861.4 nm external-cavity diode laser (TOPTICA

DL pro) for resonant excitation of the zero-phonon line (ZPL). The resonant laser frequency was stabilized using a wavemeter (HighFinesse WS-8-10) referenced to a frequency-stabilized He-Ne laser (632.991405 nm, ± 5 MHz). Each laser passed through an acousto-optic modulator to enable pulsed operation for time-resolved experiments, e.g. Ramsey sequences, and the two beams were combined on a dichroic mirror (Thorlabs DMLP805). In the confocal microscope, the excitation and collection paths were separated by a wedged beam splitter (Thorlabs BSF2550). The collected fluorescence was filtered with a 875 nm long-pass filter (Thorlabs FELH0875) so that only photons from the red-shifted phonon sideband (PSB) were detected. Single photons were recorded using a superconducting nanowire single-photon detector (Single Quantum Eos R12). Microwave (MW) control was provided by a vector signal generator (Rohde & Schwarz SMBV100A). An FPGA-based control unit (National Instrument) was used to generate timing triggers for the lasers and MW pulses and to count photon events. A static magnetic field was applied by an external permanent magnet positioned outside the cryostat.

B. Spin Hamiltonian

To model the coherent dynamics of the V1 center in 4H-SiC, whose ground state is a spin-3/2 quartet [12,13], we adopt a minimal Hamiltonian that captures the dominant energy terms and the interaction with a resonant MW drive. The spin-3/2 manifold comprises four Zeeman sublevels ($m_s = \pm 3/2, \pm 1/2$). This enlarged Hilbert space enables rich multilevel dynamics but also admits weak off-resonant excitation of non-addressed transitions, which can manifest as spectral crosstalk. We choose the crystal c-axis as the quantization axis ($z||c$). In the laboratory frame the ground state spin Hamiltonian is

$$\hat{H}_{lab} = \omega_0 \hat{S}_z + D_{gs} \left(\hat{S}_z^2 - \frac{5}{4} \right) + \omega_1 \cos(\omega t) \hat{S}_x, \quad (1)$$

where $\omega_0 = g\mu_B B_0 / \hbar$ is the Larmor frequency for a static magnetic field B_0 , $\omega_1 = g\mu_B B_1 / \hbar$ is the Rabi frequency proportional to the microwave drive amplitude B_1 , and D_{gs} denotes the ground state axial zero-field splitting parameter, i.e. $ZFS = 2D_{gs}$ for $S = 3/2$. The constant $-5D_{gs}/4$ will be omitted in the following, since it merely shifts all the spin sublevels uniformly.

Moving to the frame rotating at the drive frequency ω and applying the rotating-wave approximation [34,35] yields

$$\hat{H}_{rot} = (\omega_0 - \omega)\hat{S}_z + D_{gs}\hat{S}_z^2 + \omega_1\hat{S}_x. \quad (2)$$

Throughout, we define the detuning by $\delta \equiv \omega - (\omega_0 + 2D_{gs})$ so that $\delta > 0$ corresponds to a drive set above the $|+3/2\rangle \leftrightarrow |+1/2\rangle$ resonance frequency ($\omega_0 + 2D_{gs}$). When the B_1 drive is off during Ramsey free precession, i.e. $\omega_1 = 0$, \hat{H}_{rot} is diagonal in the $\{|+3/2\rangle, |+1/2\rangle, |-1/2\rangle, |-3/2\rangle\}$ basis with eigenvalues $E_{-3/2} = 3\delta/2 + 4D_{gs}$, $E_{-1/2} = \delta/2$, $E_{+1/2} = -\delta/2 - 2D_{gs}$, and $E_{+3/2} = -3\delta/2 - 2D_{gs}$. These level energies directly generate the detuning-dispersive frequency branches observed in the Fourier spectra via pairwise differences $\Omega_{mn} = |E_m - E_n|$ (detailed mapping appears in Sec. 3D). The explicit 4×4 matrix forms can be found in Appendix A.

C. Ramsey pulse sequence

We employ a standard Ramsey sequence, a widely used interferometric protocol in quantum information processing and quantum metrology, consisting of a $\pi/2$ pulse, a free-evolution interval τ , and a second $\pi/2$ pulse with a fixed relative phase $\phi = 0$ with respect to the first pulse [35-37]. The drive is applied at frequency ω with detuning δ . Both $V1$ and $V2$ centers are initialized into the statistical equal mixture between $|+1/2\rangle$ and $|-1/2\rangle$ of the ground state only when optical spin polarization is implemented [13]. Although the selective initialization protocol has been well established both theoretically [38] and experimentally [12], we establish the mixed state as an initial state since we aim to observe various features from the crosstalk between sublevels. However, for the analytical expressions, we assume the initialization into $|+1/2\rangle$ because it is easier to handle and sufficient to find the analytical form for phase evolution as a result of the Ramsey sequence. The overall unitary is

$$\hat{U}_{Ramsey}(\tau) = \hat{R}_x\left(\frac{\pi}{2}\right) e^{-i\hat{H}_{rot}\tau} \hat{R}_x\left(\frac{\pi}{2}\right), \quad (3)$$

where H_{rot} is defined as in Sec. 2B, which becomes diagonal during free evolution ($\omega_1 = 0$) time τ . Then, the pairwise differences in the eigenvalues of the quartet sublevels generate the detuning-dispersive components, Ω_{mn} , observed in the Fourier spectra. By applying Hard-pulse approximation, we can find the explicit form of $\hat{R}_x(\pi/2)$ (see Appendix B) which allows us to find the final state $|\psi_f\rangle$, explicitly [34]. Then, the final state projects onto

$\hat{O}_2 = | -3/2 \rangle \langle -3/2 | + | +3/2 \rangle \langle +3/2 |$ since we use O_2 optical resonance for the optical spin population readout (see Fig.1(a)) [38]. Then, the observable Ramsey signal $S(\tau, \delta) = \langle O_2 \rangle$ can be written as,

$$S(\tau) = \langle \psi_f | \hat{O}_2 | \psi_f \rangle = C_0 + \sum_{m < n} 2|X_{mn}| \cos [\Omega_{mn}t - \arg X_{mn}], \quad (4)$$

where C_0 and X_{mn} are constants determined by the initial state and the matrix elements of $\hat{R}_x(\pi/2)$. The exact definitions for X_{mn} and explicit 4×4 matrix forms of $\hat{R}_x(\pi/2)$ and the detailed derivation are provided in Appendix B. The final solution, eq.4, leads to finding six values for Ω_{mn} ,

$$\{\Omega\} = \{\delta, \delta + 2D_{gs}, \delta + 4D_{gs}, 2\delta + 2D_{gs}, 2\delta + 6D_{gs}, 3\delta + 6D_{gs}\}, \quad (5)$$

which can also be found in the experimental data as will be explained below. In practice we sweep δ at fixed B_0 and τ , compute the fast Fourier transform (FFT) of $S(\tau)$ to locate $\{\Omega_{mn}\}$, and compare the extracted peaks with the linear branches predicted above.

III. RESULTS

A. Optical resonances and coherent control of the $S = 3/2$ ground manifold

To support our crosstalk analysis of the $V1$ center's $S = 3/2$ ground-state manifold in 4H-SiC, we first establish the optical resonances used for initialization/readout and verify coherent spin control. These measurements set the model parameters for the simulations that follow and determine the experimental settings required for high-visibility Ramsey measurements. We operate at $T \approx 5$ K so that photoluminescence-excitation (PLE) spectra approach the lifetime-limited regime, enabling clean resolution of two spin-preserving ($\Delta m_S = 0$) and spin-selective ZPL resonances [12,39].

We locate these lines by scanning the laser across the ZPL while monitoring PSB emission. As shown in Fig. 1b, the PLE spectrum exhibits two narrow resonances separated by ≈ 1 GHz, consistent with the excited-state zero-field splitting D_{es} [11,12,39,40]. Under weak resonant excitation, the narrowest observed linewidth is 340 MHz (FWHM), approaching the lifetime-limited value for this color center [12]. In our notation, O_1 denotes the pair $| g, m_S = \pm 1/2 \rangle \leftrightarrow | e, m_S = \pm 1/2 \rangle$ and O_2 denotes $| g, m_S = \pm 3/2 \rangle \leftrightarrow | e, m_S = \pm 3/2 \rangle$ (see Fig. 1a) [40].

These observations are consistent with a stable charge state under our conditions and minimal inhomogeneous broadening from nearby defects [11,41].

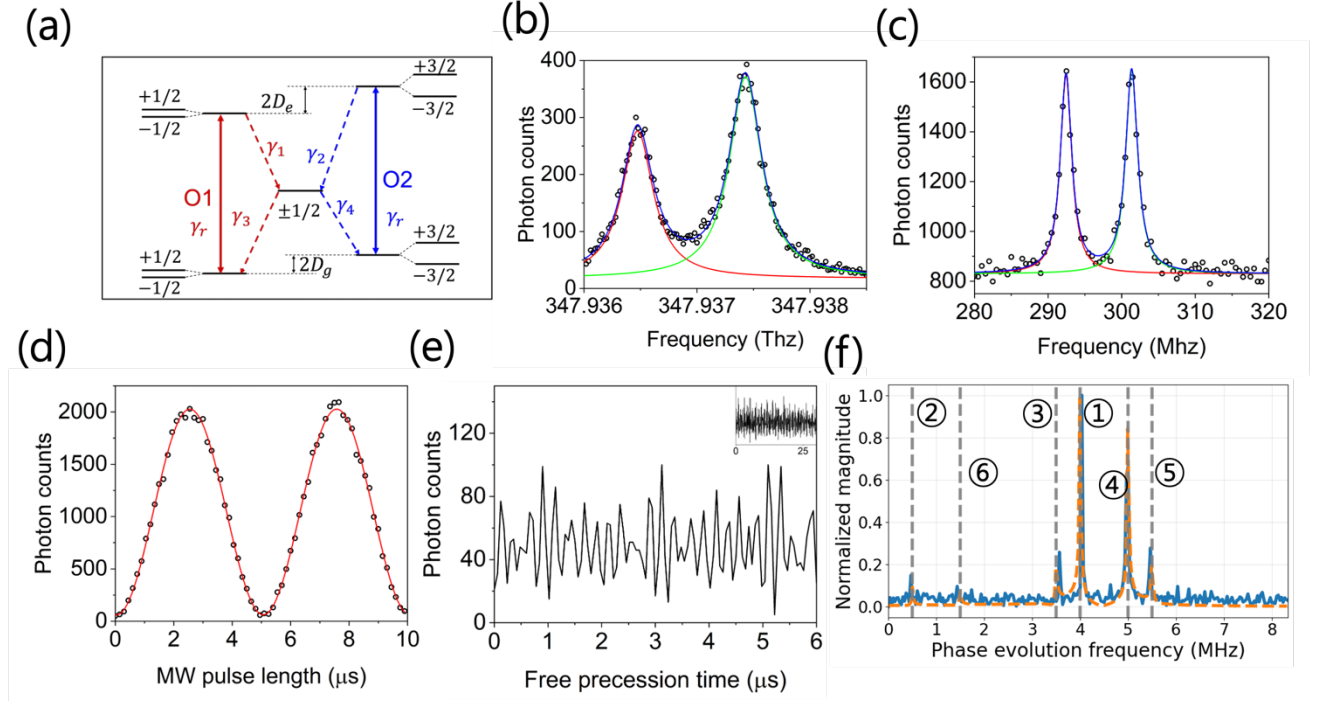


FIG. 1. (a) Level diagram and rate model of the V_1 center in 4H-SiC ($O_1: m_S = \pm 1/2$, $O_2: m_S = \pm 3/2$). γ_r is the radiative transition rate, while γ_1 , γ_2 , γ_3 , and γ_4 are non-radiative ISC rates [38]. (b) PLE spectrum of the V_1 center measured at $T \approx 5$ K and without an external magnetic field. The solid lines are Lorentzian fit. (c) cw-ODMR with the laser parked on O_2 under a static field of 100 G parallel to c-axis. The solid lines are Lorentzian fit. (d) Optically detected Rabi oscillations measured under resonant microwave driving at $m_S = +3/2 \leftrightarrow m_S = +1/2$ with a sinusoidal fit (solid line). (e) A zoom-in of the Ramsey fringes from two $\pi/2$ pulses separated by τ with detuning $\delta/2\pi = -4$ MHz. The inset is the same data in the full range of the free-precession time involved. (f) FFT of the Ramsey fringes (blue solid line), showing multiple frequency components induced by crosstalk between spin transitions. The simulation (orange dashed line), and the numbered frequency positions labeled by ①–⑥ are discussed in III.B, C, and D.

Figure 1a also schematizes the rate model used throughout: a minimal three-manifold scheme with the ground quartet, the excited quartet, and a metastable shelving manifold. Optical driving on O_1/O_2 is treated as predominantly $\Delta m_S = 0$ (spin-conserving) transition, while spin-dependent intersystem-crossing (ISC) pathways

via the metastable state provide the effective spin-flip channel that redistributes population between $|m_S = \pm 1/2\rangle$ and $|m_S = \pm 3/2\rangle$ [38,42]. In practice, O_1 (O_2) pumping tends to polarize the ground state toward $|m_S = \pm 3/2\rangle$ ($|m_S = \pm 1/2\rangle$) via ISC; this mechanism underlies the initialization protocols used for ODMR [38,39].

To characterize the ground-state spin resonances, we perform continuous-wave ODMR with a constant external magnetic field of 104.80(4) G aligned to the c-axis. With a narrow-linewidth laser fixed on O_2 , we scan the MW frequency while recording the PSB fluorescence. Under continuous O_2 pumping, spin-dependent intersystem crossing (ISC) depletes the $m_S = \pm 3/2$ sublevels and accumulates population in the $m_S = \pm 1/2$ manifold (a mixed state of the two sublevels) [8,12,38]. At MW resonance, the drive induces the $\Delta m_S = \pm 1$ transitions that transfer population from $m_S = \pm 1/2$ into $m_S = \pm 3/2$. Because those sublevels are directly addressed by O_2 , the photon emission rate rises sharply, yielding high-visibility ODMR contrast. Although near-pure state initialization into a single m_S sublevel is achievable with resonant pumping with broadband MW excitation [12,38], our focus here is crosstalk in the $S = 3/2$ manifold. For this purpose, initialization into the mixed $m_S = \pm 1/2$ manifold is sufficient and operationally simpler, and we adopt it throughout. The resulting spectrum (Fig. 1c) shows two distinct lines corresponding to the outer $\Delta m_S = \pm 1$ transitions $m_S = \pm 3/2 \leftrightarrow \pm 1/2$ with the absence of the middle transition $m_S = -1/2 \leftrightarrow +1/2$ in agreement with the well-known $V1$ ground-manifold structure [12].

[38]. With the optical and MW resonances identified, we measure spin Rabi oscillations to set the pulse parameters for coherent control. For the high visibility Rabi observations, we initialized into a near pure state of $m_S = +1/2$ by implementing the selective initialization protocol [38]. With a narrow-linewidth laser fixed on O_2 and the MW tuned to the resonance at $m_S = +3/2 \leftrightarrow +1/2$, we observe high-contrast, optically detected Rabi oscillations (Fig. 1d). A damped-sine fit yields a maximum visibility of 95(1)% and the $\pi/2$ -pulse duration at the chosen MW power which is used throughout. These calibrations set the pulse parameters for the broadband Ramsey interferometry presented next, where we quantify crosstalk among the $S = 3/2$ sublevels.

We next implement a Ramsey pulse sequence to probe the phase evolution and frequency response of the $S = 3/2$ spin system with $\omega_1/2\pi = 3.125$ MHz. Two 80 ns long $\pi/2$ MW pulses are applied, separated by a variable free-precession interval τ . The MW was detuned by -4 MHz from the chosen outer transition, $m_S = +3/2 \leftrightarrow$

$\pm 1/2$, so that the phase accumulates at 4 MHz during free precession. The second $\pi/2$ pulse maps this accumulated phase to population for optical readout [37]. A representative time-domain trace (Fig. 1e) shows fringes that do not reduce to a single-frequency sinusoid; instead, visible multi-frequency modulation is observed. To make the frequency content explicit, we compute the FFT of the Ramsey signal (Fig. 1f). In addition to the 4 MHz component by the programmed detuning, the spectrum exhibits additional strong peaks at around 3.5 MHz, 5 MHz and 5.5 MHz and two more small peaks with marginal SNR ratio at around 1 MHz and 1.5 MHz that cannot be accounted for by a two-level model. These features indicate coherent crosstalk among multiple spin transitions within the $S = 3/2$ manifold. In what follows, we develop a multi-transition theoretical framework to quantitatively reproduce the Ramsey spectra and isolate the crosstalk pathways.

B. Numerical prediction of multilevel Ramsey branches

Motivated by the multi-frequency Ramsey response in Fig. 1e–f, we numerically simulate the Ramsey sequence to preview the frequency branches expected from a four-level $S = 3/2$ manifold under our experimental conditions. All simulations were implemented in Wolfram Mathematica using the SpinDynamica package, which provides a density-matrix/Schrödinger-equation simulation framework for driven spin dynamics[43]. The simulations integrate the time-dependent Schrödinger equation in the rotating frame using the Hamiltonian of Eq. (2) (see Sec. II and Appendix A). We mirror the experimental initialization (mixed $m_S = \pm 1/2$ ground manifold), apply a $\pi/2$ pulse with the detuning $\delta/2\pi$, allow free precession for a variable interval τ , and apply a final $\pi/2$. The measured quantity is the O_2 readout channel, modeled by the measurement operator \hat{O}_2 , $S(\tau) = \langle \psi_f | \hat{O}_2 | \psi_f \rangle$. To isolate spectral content cleanly, we use idealized conditions (long acquisition window and dense sampling) beyond what is available experimentally.

Figure 2 shows the numerical simulations for the detuning-dependent Ramsey spectra obtained by sweeping the MW detuning $\delta/2\pi$ while holding the drive amplitude ω_1 fixed ($\omega_1/2\pi = 5$ MHz) which is intentionally chosen to be a little larger than the experimental value in order to not miss any important features. Under these idealized conditions, the Fourier transform reveals six branches, rather than a single line at $|\delta/2\pi|$ which tells us that the

multi-frequency features found in the experimental data as in Fig.1(f) are not artifacts but capture the nature of the ququart. As detailed in Appendix B, these components correspond to pairwise coherences between the four m_s sublevels. The relative amplitudes of these branches are governed by the prepared initial state and by δ and ω_1 which will be explained in III.C. The resulting map reproduces the multi-peak structure seen in Fig.1(f) and motivates a compact physical assignment.

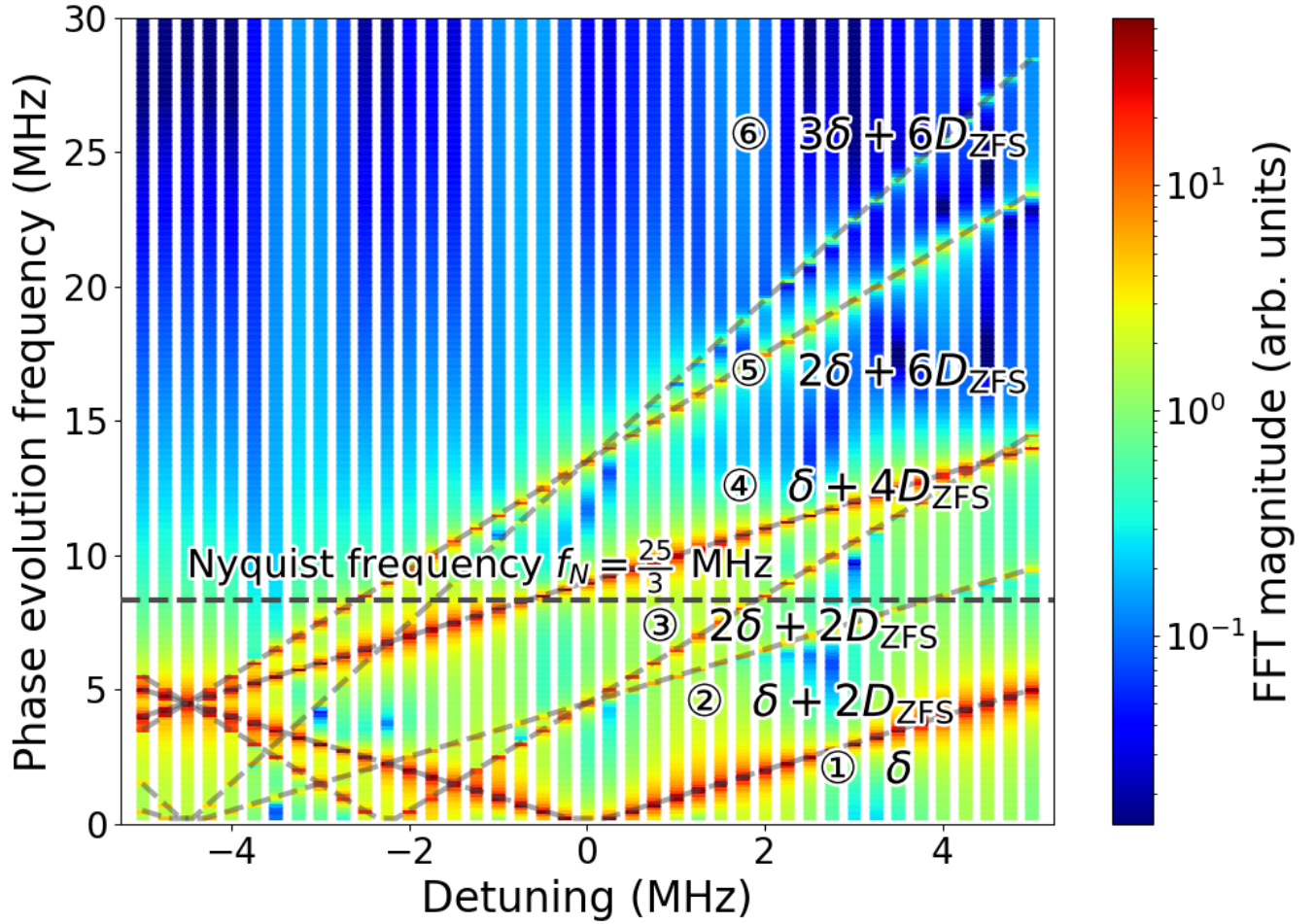


FIG. 2. Simulated Ramsey branch map. FFT magnitude (color) in logscale versus detuning $\delta/2\pi$ for the addressed $m_s = +3/2 \leftrightarrow +1/2$ transition at fixed ω_1 . Six branches (①–⑥) are visible; gray dashed red lines are the analytic branch expressions from III.C overlaid on the simulation. The spectral branches are ordered and labeled starting from the lowest frequency components generated at small detuning $|\delta|$. The horizontal dashed line at around 8.3 MHz indicates the Nyquist frequency f_N set by the experimental Ramsey sampling interval, above which spectral components are subject to aliasing.

To develop intuition for the multicomponent Ramsey spectra, we visualize the four-level dynamics on two-level Bloch-sphere subspaces extracted from the $S = 3/2$ manifold. While the full evolution unfolds in a four-dimensional Hilbert space, projecting onto selected pairs provides a geometric picture of how detuned $\pi/2$ pulses seed coherences beyond the targeted transition and how free precession redistributes phase. Figure 3 shows illustrative trajectories of the Bloch vectors under a resonant hard pulse followed by free evolution for three representative neighbor pairs.

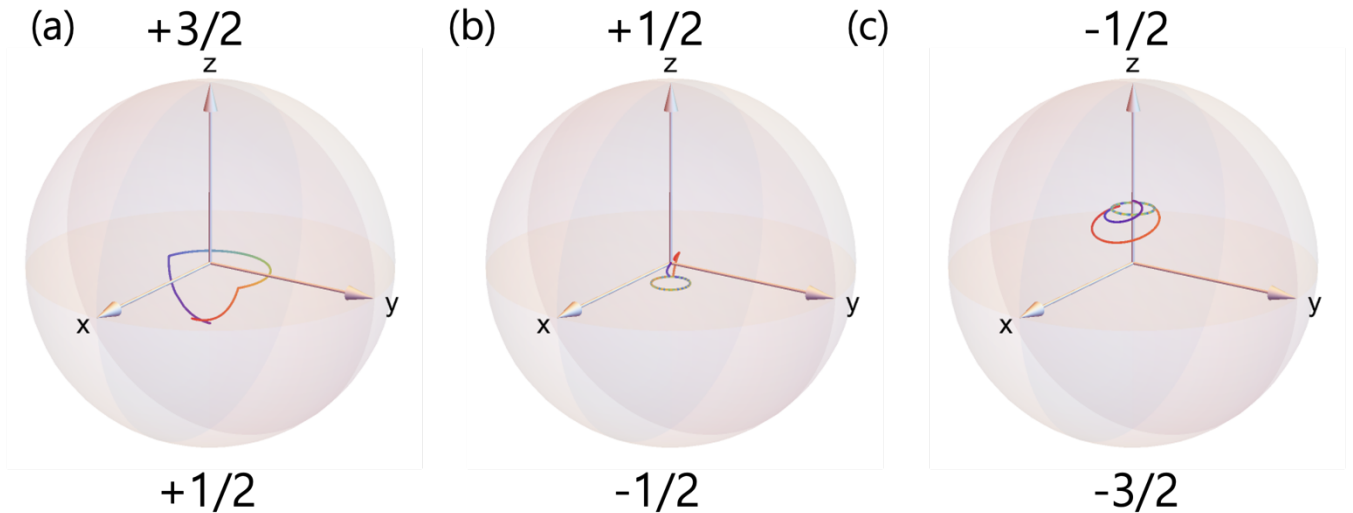


FIG. 3. Bloch-sphere trajectories for a Ramsey sequence driven with resonant hard $\pi/2$ pulses on the outer transition ($m_s = +3/2 \leftrightarrow +1/2$) at $\delta/2\pi = 1$ MHz. Panels: (a) subspace $\{+3/2, +1/2\}$, (b) $\{+1/2, -1/2\}$, (c) $\{-1/2, -3/2\}$. The trajectory starts at the purple point and evolves toward the red point, and the surface corresponds to the unit length.

Figure 3 (a) depicts the addressed outer pair, $| +3/2 \rangle \leftrightarrow | +1/2 \rangle$. Starting near the south pole set by the optical initialization, the first $\pi/2$ pulse rotates the Bloch vector to the equator, creating a superposition of the two sublevels. During the subsequent free precession, the Bloch vector winds around the z -axis at a rate set by the detuning $\delta/2\pi$, reproducing the familiar single-pair Ramsey mechanism. If the system were strictly two-level, the trajectory would remain confined to this sphere and the time-domain signal would be close to a single-frequency sinusoid. Panels (b) and (c) show the middle and opposite outer single-quantum pairs, $| +1/2 \rangle \leftrightarrow | -1/2 \rangle$ and $| -1/2 \rangle \leftrightarrow | -3/2 \rangle$, respectively. Although these pairs are not directly resonant with the applied drive, the finite spectral bandwidth of

the short pulses (e.g., 50 ns in this simulation) and the multilevel couplings induce weak, off-resonant rotations that generate residual coherences in these subspaces. As a result, their Bloch vectors depart from the poles and trace small but coherent trajectories. These secondary motions seed additional Fourier components in the Ramsey signal once the accumulated phases are projected back to populations by the second $\pi/2$ pulse and read out on O_2 . Thus, even with a drive nominally targeting a single outer transition, coherence is not confined to one two-level manifold. In what follows we refer to these off-resonant pathways into non-addressed pairs as spectator transitions. Taken together, the three Bloch-sphere projections in Fig. 3 provide a dynamical picture consistent with the numerical branch map: the Ramsey sequence excites coherences in multiple neighbor pairs, leading to a spectrum with several lines rather than a single detuning component. This visualization is intended as an intuitive guide; a quantitative assignment of branch frequencies and their weights in terms of pairwise coherences is given in Appendix B and used in the analytical treatment that follows.

C. Analytical frequency set and mapping

Guided by the numerical preview in III.B, we now state the analytic frequency set for the Ramsey response of the $S = 3/2$ manifold. In the rotating frame (Eq. (2)), the free-evolution phases are governed by the level energies E_m and the Ramsey signal takes the form (see Appendix B for detail)

$$S(\tau) = S_0 + \sum_{m < n} 2|X_{mn}| \cos(\Omega_{mn}\tau - \arg X_{mn}), \quad (6)$$

where each of the six coherences (m, n) in the $S = 3/2$ manifold contributes a cosine at a frequency $\Omega_{mn}/2\pi$ and with a weight $|X_{mn}|$ set by the prepared state and the $\pi/2$ pulse matrix (see Appendix B). The underlying frequencies $\{\Omega_{mn}/2\pi\}$ are the six pairwise energy splittings of the rotating-frame Hamiltonian as in eq.(5) and are listed and labeled in Fig. 2 as branches ①–⑥ (ordered by increasing frequency at small $|\delta/2\pi|$). That labeling is

used throughout this section and in Fig. 4. For clarity, except the branch associated with the addressed outer single-quantum pair with $\Omega_{+1/2,+3/2} = \delta$, all the remaining components originating from off-resonant pairs are ‘spectator-transition branches’ that acquire coherence during the sequence. Because the data (and the simulations in Fig. 4) are sampled with a sampling rate $f_s = 1/(60 \text{ ns})$, only the first Nyquist zone $[0, f_N]$ with the Nyquist

frequency $f_N \equiv f_s/2$ is observable as in Fig.4 a,b [44,45]. As an example, the unaliased phase evolution frequency of the branch ③ is $\Omega_{-3/2,-1/2}/2\pi = (2\delta + 2D_{gs})/2\pi$ when $\delta/2\pi \leq (f_N - 2D_{gs}/2\pi)/2$ but the aliased frequency becomes $\Omega_{-3/2,-1/2}/2\pi = 2f_N - (2\delta + 2D_{gs})/2\pi$ when $\delta/2\pi > (f_N - 2D_{gs}/2\pi)/2$ due to the Nyquist folding (mirror about f_N) as in Fig.4a,b. Another example is the frequency of the branch ⑥ $\Omega_{-3/2,+3/2}/2\pi = (3\delta + 6D_{gs})/2\pi$ of which unaliased frequency does not fall in the first Nyquist zone even at the zero detuning. In the end, it shows the folding three times in the considered frequency range in Fig.4 a,b; $\Omega_{-3/2,+3/2}/2\pi = 2f_N - (3\delta + 6D_{gs})/2\pi$ when $\delta/2\pi \leq (2f_N - 6D_{gs}/2\pi)/3$, $-2f_N + (3\delta + 6D_{gs})/2\pi$ when $(2f_N - 6D_{gs}/2\pi)/3 < \delta/2\pi \leq f_N - 2D_{gs}/2\pi$, and $4f_N - (3\delta + 6D_{gs})/2\pi$ when $\delta/2\pi > f_N - 2D_{gs}/2\pi$ [45]. The set of six observed frequencies in the simulations of Fig. 4 a,b is precisely the image of the unaliased $\{\Omega_{mn}/2\pi\}$ under this map; the branch identities (①–⑥) are preserved continuously through the folds. The positions are fully determined by the level spacings (Sec. II), while the relative amplitudes are set by the prepared initial state and by δ and ω_1 via the pulse matrix (Appendix B). This frequency mapping explains the multi-ridge structure of the detuning sweep and the apparent “reflections” where lines cross the Nyquist boundary.

D. Quantitative comparison with experiment

We now benchmark the model against the Ramsey measurements at the various detuning frequencies used experimentally. Figures 4c–d overlay the experimental FFT with the numerical spectrum computed under the same acquisition window and sampling as the data, and with the analytic frequency ticks (vertical markers) for branches ①–⑥. The only inputs are the calibrated parameters from §III.A (resonant frequencies, $\pi/2$ pulse), the fixed drive amplitude $\omega_1/2\pi=3.125$ MHz, and the working detuning varies between $\delta/2\pi = -4$ and 3 MHz; no additional parameter is introduced other than an overall vertical scale.

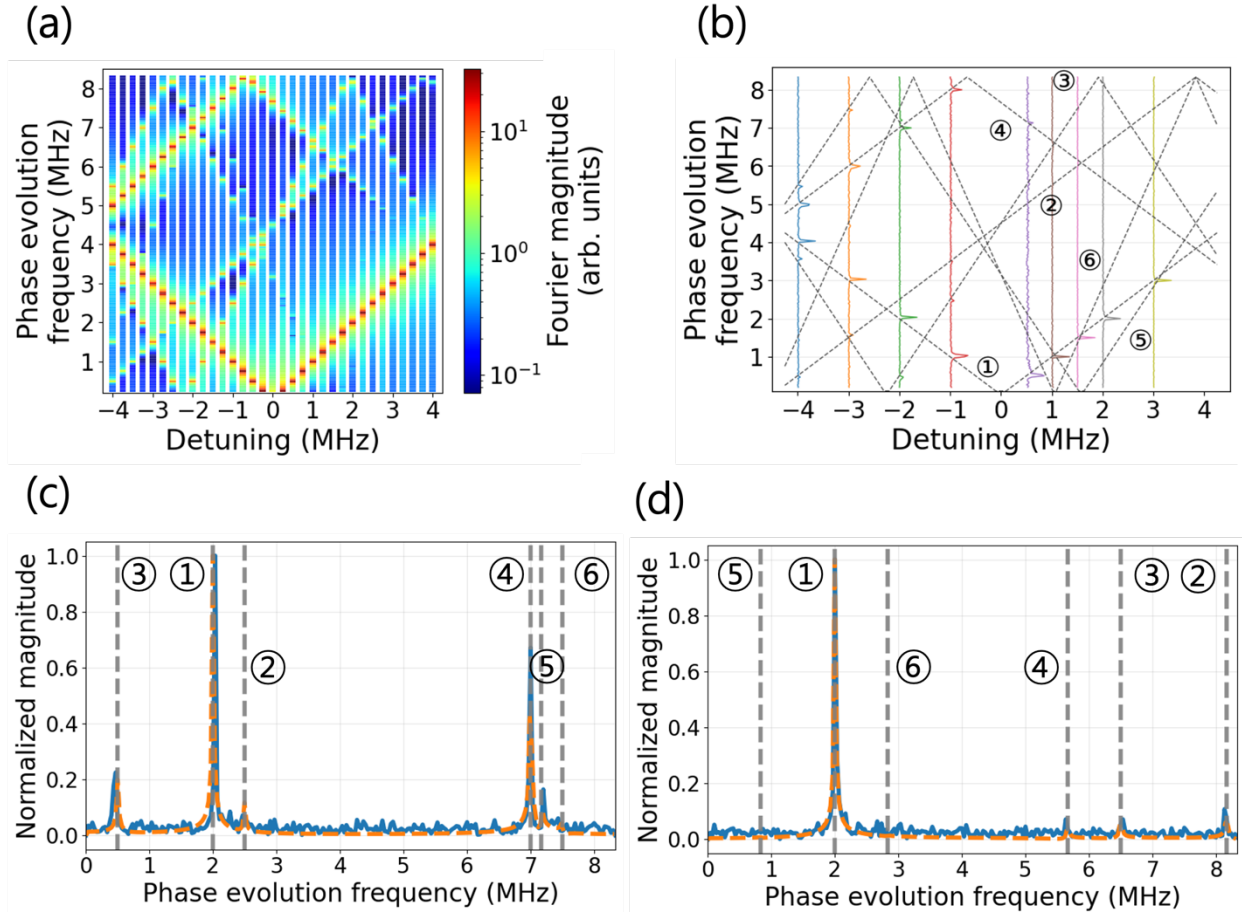


FIG. 4. (a) Detuning sweep under experimental sampling. Fourier amplitude from numerical simulation in logscale as a function of detuning $\delta/2\pi$ using the same experimental parameters including the fixed drive ω_1 , time step $\Delta\tau$ and window as the experiment. (b) Experimental Ramsey data, shown as the normalized magnitude of the extracted phase-evolution frequencies, vertically offset and plotted as a function of detuning. (c) Experimental (blue solid lines) and simulated (orange dashed lines) spectra at a detuning of -2 MHz, (d) +2 MHz. For (c), and (d), the six branches ①–⑥ found by analytic solutions are indicated as well.

Across the used detunings, the peak positions in the FFT follow the analytic frequency set after Nyquist folding (cf. §III.C): components that cross the Nyquist boundary appear mirrored about f_N , and the data peaks track these folded ticks within the frequency resolution set by the acquisition window. This one-to-one agreement confirms the six-branch structure predicted for a spin-3/2 Ramsey sequence and validates the branch labels defined in Fig. 2 and used throughout Fig. 4. The relative amplitudes of the branches are reproduced qualitatively by the numerics:

components associated with the addressed outer single-quantum pair dominate, while additional lines, originating from coherences in other pair subspaces, appear with smaller but repeatable weights. Differences in absolute height are expected because the amplitudes depend on the prepared mixture within $m_S = \pm 1/2$, the exact pulse area and phase at the working power, windowing/apodization of the time trace, and dephasing over the acquisition (T_2^*); these effects are only approximately captured by the simple simulation used for Fig. 4. Importantly, the set and locations of the peaks require no free parameters beyond those already calibrated.

Taken together, Figure 4 shows that the experiment, the numerical time-domain propagation, and the analytical mapping all point to the same picture: the Ramsey response of the V1 center's $S = 3/2$ manifold comprises six well-defined spectral branches, with positions fixed by the level spacings and detuning, and weights governed by the prepared state and pulse parameters.

IV. CONCLUSIONS

We have shown that Ramsey interferometry on the V1 center's $S = 3/2$ manifold yields a deterministic six-component spectrum that reflects pairwise coherences across the four spin sublevels. Starting from spin-selective resonant optics (O_1/O_2) and coherent control, we measured high-visibility Ramsey traces whose Fourier spectra contain multiple lines. A compact analytical description connects each observed frequency Ω_{mn} to a specific sublevel pair (m, n) and assigns its weight to the complex amplitude $|X_{mn}|$ determined by the prepared state and the two $\pi/2$ pulses. Numerical propagation under experimental sampling reproduces the full detuning map, including Nyquist-folded features, and the experimental FFT peaks coincide with the analytic frequency ticks without additional fitting for peak positions.

Short finite-bandwidth $\pi/2$ pulses seed coherences not only in the addressed transition but also via spectator transitions, off-resonant sublevel pairs that acquire small yet coherent amplitudes during the sequence. The second $\pi/2$ pulse projects all accumulated phases onto the O_2 readout, so the Ramsey signal becomes a weighted superposition of six pair coherences. In this regime, crosstalk is intrinsic, not a minor imperfection of the measurement.

Practically, the framework provides clear guidance for control: branch positions are fixed by the level spacings and detuning, while branch weights $|X_{mn}|$ can be tuned through initialization and the pulse parameters $(\delta, \omega_1, \tau_p)$. These insights can be used to suppress crosstalk by choosing more selective pulses and detunings, or to exploit it, for example, by deliberately populating spectator transitions to increase informational content for quantum state/process tomography or other forms of state estimation based on the set of measured amplitudes and phases.

Beyond the specific defect studied here, the analysis and mapping generalize to multilevel qudits: in any spin manifold, Ramsey frequency content is determined by energy differences between sublevels, so the approach immediately predicts which spectral components can appear and how they fold under finite sampling. Looking ahead, the methodology invites systematic exploration of pulse parameter regimes that minimize or shape crosstalk, and motivates studies of how spectator transitions impact Hahn-echo and broader dynamical-decoupling sequences. It also suggests using the $|X_{mn}|$ structure to design tomography/estimation protocols that reconstruct either the prepared state or pulse-induced unitary *in situ* from the multi-component Ramsey response. Together, these elements provide a quantitative and portable description of multilevel Ramsey physics, enabling both more robust control and new metrological opportunities in qudit platforms.

ACKNOWLEDGMENTS

JWH acknowledges support from the Swedish Research Council (VR) (Grant No. 2020-05444) and the European Union under Horizon Europe for the project SPINUS (Grant No. 101135699). NTS acknowledges support from the European Union under Horizon Europe for projects QuSPARK (Grant No. 101186889), QRC-4-ESP (Grant No. 101129663), and QUEST (Grant No. 101156088), and from Vinnova (Grant No. 2024-00461, and 2025-03848), QUASIC within QSIP project (Grant No. 2024-03597). JWH and NTS acknowledge support from the Knut and Alice Wallenberg Foundation (Grant No. KAW 2018.0071). JKS acknowledges that this work was supported by the KOMAC operation fund of KAERI by MSIT (Ministry of Science and ICT). This work was supported by the Institute of Information & communications Technology Planning & Evaluation (IITP) grant (II220198, RS-2025-02306096), and the National Research Foundation of Korea (NRF) (2021R1A2C2006904, 2022M3H3A106307411) funded by the Korean government (Ministry of Science and ICT).

APPENDIX A: Details for §II.B : Spin Hamiltonian

A1. Basis, symbols, and detuning convention

We use the ordered \hat{S}_z basis $\{|+3/2\rangle, |+1/2\rangle, |-1/2\rangle, |-3/2\rangle\}$, set $\hbar = 1$, and parameterize the axial zero-field splitting (ZFS) of a spin-3/2 manifold with $ZFS = 2D_{gs}/2\pi$. A constant offset $-5D_{gs}/4$ shifts all eigenenergies equally and is dropped everywhere. We follow the §II.B detuning convention $\delta \equiv \omega - (\omega_0 + 2D_{gs})$, so that $\delta > 0$ corresponds to a drive set above the $|+3/2\rangle \leftrightarrow |+1/2\rangle$ resonance at $\omega_0 + 2D_{gs}$.

A2. Explicit 4×4 matrix of the rotating frame Hamiltonian

In the ordered basis above, the spin-3/2 operators are

$$S_z = \begin{pmatrix} \frac{3}{2} & 0 & 0 & 0 \\ 0 & \frac{1}{2} & 0 & 0 \\ 0 & 0 & -\frac{1}{2} & 0 \\ 0 & 0 & 0 & -\frac{3}{2} \end{pmatrix}, \quad S_x = \frac{1}{2} \begin{pmatrix} 0 & \sqrt{3} & 0 & 0 \\ \sqrt{3} & 0 & 2 & 0 \\ 0 & 2 & 0 & \sqrt{3} \\ 0 & 0 & \sqrt{3} & 0 \end{pmatrix}, \quad S_y = \frac{1}{2i} \begin{pmatrix} 0 & \sqrt{3} & 0 & 0 \\ -\sqrt{3} & 0 & 2 & 0 \\ 0 & -2 & 0 & \sqrt{3} \\ 0 & 0 & -\sqrt{3} & 0 \end{pmatrix}. \quad (A1)$$

These matrices explain the unequal transverse couplings: $|\pm 3/2\rangle \leftrightarrow |\pm 1/2\rangle$ carry $\sqrt{3}/2$, whereas $|+1/2\rangle \leftrightarrow |-1/2\rangle$ carries 1. Hence, from eq (2) in the main text

$$\hat{H}_{rot} = \begin{pmatrix} D_{gs} + \frac{3}{2}(\omega_0 - \omega) & \frac{\sqrt{3}}{2}\omega_1 & 0 & 0 \\ \frac{\sqrt{3}}{2}\omega_1 & -D_{gs} + \frac{1}{2}(\omega_0 - \omega) & \omega_1 & 0 \\ 0 & \omega_1 & -D_{gs} - \frac{1}{2}(\omega_0 - \omega) & \frac{\sqrt{3}}{2}\omega_1 \\ 0 & 0 & \frac{\sqrt{3}}{2}\omega_1 & D_{gs} - \frac{3}{2}(\omega_0 - \omega) \end{pmatrix}. \quad (A2)$$

A3. Free-evolution spectrum and the six Ramsey frequencies

With the drive off ($\omega_1 = 0$) during the free-precession, the free Hamiltonian is diagonal:

$$\hat{H}_{free} = (-\delta + 2D_{gs})\hat{S}_z + D_{gs}\hat{S}_z^2, \quad (A3)$$

with the eigenvalues

$$E_{-3/2} = \frac{3}{2}\delta + 4D_{gs}, E_{-1/2} = \frac{\delta}{2}, E_{+1/2} = -\frac{\delta}{2} - 2D_{gs}, E_{+3/2} = -\frac{3}{2}\delta - 2D_{gs}. \quad (A4)$$

All pairwise differences $\Omega_{mn} = |E_m - E_n|$ yield the six detuning-dispersive components observed in Figs. 2 and 4,

$$\{\Omega\} = \{\delta, \delta + 2D, \delta + 4D, 2\delta + 2D, 2\delta + 6D, 3\delta + 6D\}. \quad (\text{A5})$$

These frequency components will also be directly derived from the observables, $S(\tau) = \langle \psi_f | \hat{O}_2 | \psi_f \rangle$, as in Appendix B.

APPENDIX B: Details for §II.C : Ramsey sequence and frequency decomposition

B1. Sequence, initial state, and measurement

We model the Ramsey sequence by

$$\hat{U}_{\text{Ramsey}}(\tau) = \hat{R}_x\left(\frac{\pi}{2}\right) e^{-i\hat{H}_{\text{free}}\tau} \hat{R}_x\left(\frac{\pi}{2}\right), \quad (\text{B1})$$

where H_{free} is the free-evolution Hamiltonian in Appendix A, $\hat{R}_x(\pi/2)$ are the first/second $\pi/2$ pulses (general 4×4 unitaries) of which relative MW phases are zero. τ is free-precession time in which ω_1 is off. The initial state ρ_0 is set to be a pure state $|+1/2\rangle$. Although the V1 center in this work is initialized into the equal statistical mixture of $|\pm 1/2\rangle$ [38], this assumption will allow to simplify the problem so that we can find the solution for the frequency components of the time-evolution by the used Ramsey sequence. Note that our interest is to understand the origin of the phase evolution frequency and its relation to the detuning.

We read out the signal

$$S(\tau) = \text{Tr}[\hat{O}_2 \hat{U}_R(\tau) \rho_0 \hat{U}_R^\dagger(\tau)], \quad (\text{B2})$$

with the default choice $\hat{O}_2 = |+3/2\rangle\langle +3/2| + |-3/2\rangle\langle -3/2|$, consistent with the experimental observable corresponding to the O_2 transition. The other observable $\hat{O}_1 = |+1/2\rangle\langle +1/2| + |-1/2\rangle\langle -1/2|$ only reweight amplitudes but do not create new frequency branches since $\langle O_1 \rangle + \langle O_2 \rangle = 1$.

B2. Free- evolution spectrum and the six branches

As explained in A3, the free-evolution eigenenergies in the rotating frame read four different values so that observable frequencies are all pairwise differences Ω_{mn} (six in total). Using the detuning and ZFS conventions

(ZFS= $2D_{gs}$) one obtains the following six linear branches (slope–intercept form with respect to δ) as mentioned in A3 and summarized in Table 1. These six branches are exactly the detuning-dispersive components used to annotate Figs. 2 and 4 in the main text.

Table 1. During the Ramsey free-evolution the pairwise differences $\Omega_{mn} = |E_m - E_n|$ of the diagonal energies generate six linear branches as functions of detuning δ . The table lists the branch labels (①–⑥) used in Figs. 2 and 4, the analytic forms of $\Omega_{mn}(\delta)$, their slope–intercept pairs, and the (m, n) pairs in the ordered basis $\{| +3/2\rangle, | +1/2\rangle, | -1/2\rangle, | -3/2\rangle\}$.

Branch	Pair (m, n)	(slope, intercept)	$\Omega_{mn}(\delta)$
①	$(+\frac{1}{2}, +\frac{3}{2})$	$(1, 0)$	δ
②	$:(-\frac{1}{2}, +\frac{1}{2})$	$(1, 2D_{gs})$	$\delta + 2D_{gs}$
③	$:(-\frac{1}{2}, +\frac{3}{2})$	$(2, 2D_{gs})$	$2\delta + 2D_{gs}$
④	$:(-\frac{1}{2}, -\frac{3}{2})$	$(1, 4D_{gs})$	$\delta + 4D_{gs}$
⑤	$:(-\frac{3}{2}, +\frac{1}{2})$	$(2, 6D_{gs})$	$2\delta + 6D_{gs}$
⑥	$:(-\frac{3}{2}, +\frac{3}{2})$	$(3, 6D_{gs})$	$3\delta + 6D_{gs}$

B3. From the first $\pi/2$ pulse to the Ramsey signal

A general (detuned, finite-bandwidth) first $\pi/2$ pulse makes all four components non-zero. We therefore do not write the pulse matrix explicitly here and simply denote the post-pulse state as

$$|\psi_1\rangle \equiv \begin{pmatrix} c_1 e^{i\Delta_1} \\ c_2 e^{i\Delta_2} \\ c_3 e^{i\Delta_3} \\ c_4 e^{i\Delta_4} \end{pmatrix}, \quad (\text{B3})$$

with real $c_k \geq 0$ and pulse-accumulated phases Δ_k . During the free-precession interval, since H_{free} is diagonal as explained in A3, the state right before the second $\pi/2$ pulse, i.e. $e^{-i\hat{H}_{free}\tau} |\psi_1\rangle$ is, using the eigenvalues in eq. (A4) and dropping a global phase term,

$$\begin{pmatrix} c_1 e^{i\Delta_1} e^{i\delta\tau} \\ c_2 e^{i\Delta_2} \\ c_3 e^{i\Delta_3} e^{-i(\delta+2D_{gs})\tau} \\ c_4 e^{i\Delta_4} e^{-i(2\delta+6D_{gs})\tau} \end{pmatrix}. \quad (\text{B4})$$

To find the explicit form of the ququart state right after the second $\pi/2$ pulse, we investigate the full 4×4 matrix form. To expose the structure of the second $\pi/2$ pulse, it is useful to show the ideal hard-resonant rotation about x-axis for spin-3/2. During a short and high-power MW pulse of which time scale is τ_p we work in the rotating frame and neglect the internal/free Hamiltonian H_{free} while the pulse is on; the control Hamiltonian dominates. “Hard” means the MW field amplitude ω_1 is large and the pulse is brief so that evolution under H_{free} is negligible over the pulse ($\tau_p \ll 1/|H_{free}|$). “Resonant” means the drive is on resonance with the targeted transitions (detuning $\delta = 0$), so in the rotating-wave approximation the effective Hamiltonian during the pulse is $\omega_1 \hat{\sigma}_x$. Consequently, the pulse implements a pure spin-3/2 rotation about x-axis:

$$\hat{U}_p(\omega_1 \tau_p) = e^{-i\omega_1 \tau_p \hat{\sigma}_x} \equiv \hat{R}_x(\omega_1 \tau_p). \quad (\text{B5})$$

Note that these are standard magnetic resonance control assumptions: on-resonance RWA plus the “hard-pulse” approximation that internal terms (e.g., Zeeman offsets) can be ignored during τ_p . During a pulse of duration τ_p we neglect the zero-field splitting D_{gs} (hard-pulse approximation) but keep a static detuning δ to keep the generality. With Rabi amplitude ω_1 the effective Hamiltonian is

$$\hat{H}_p = -(\delta + 2D_{gs}) \hat{S}_z + \omega_1 \hat{S}_x = \Omega_{Rabi} (\hat{S}_z \cos \beta + \hat{S}_x \sin \beta) = \Omega_{Rabi} e^{-i\beta \hat{S}_y} \hat{S}_z e^{+i\beta \hat{S}_y}, \quad (\text{B6})$$

where the effective Rabi rate Ω_{Rabi} and tilt angle β are defined as

$$\Omega_{Rabi} \equiv \sqrt{(\delta + 2D_{gs})^2 + \omega_1^2}, \cos \beta = \frac{-(\delta + 2D_{gs})}{\Omega_{Rabi}}, \sin \beta = \frac{\omega_1}{\Omega_{Rabi}}. \quad (\text{B7})$$

Then, the time evolution operator is

$$\hat{U}_p(\tau_p) = \exp[-i(\delta S_z + \omega_1 S_x)\tau_p] = \exp[-i\Omega_{Rabi}\tau_p (e^{+i\beta \hat{S}_y} \hat{S}_z e^{-i\beta \hat{S}_y})] = e^{+i\beta \hat{S}_y} e^{-i\Omega_{Rabi}\tau_p \hat{S}_z} e^{-i\beta \hat{S}_y}, \quad (\text{B8})$$

where we used the similarity rule for operator exponentials, $e^{\hat{U}^\dagger \hat{A} \hat{U}} = \hat{U}^\dagger e^{\hat{A}} \hat{U}$ (with $\hat{U} = e^{-i\beta \hat{S}_y}$, $\hat{A} = -i\Omega_{Rabi} \tau_p \hat{S}_z$). Note that the final form in eq. (B8) is not the standard z-y-z Euler decomposition. Here, since Wigner D-matrix is defined as $\hat{D}^{(j)}(\alpha, \beta, \gamma) = e^{-i\alpha \hat{S}_z} e^{-i\beta \hat{S}_z} e^{-i\gamma \hat{S}_z}$ with $j = 3/2$, we express $U_p(\tau_p)$ using the products of Wigner-D matrices[46] for three rotations as

$$\begin{aligned} \hat{U}_p(\tau_p) &= \hat{D}^{\left(\frac{3}{2}\right)}(0, -\beta, 0) \hat{D}^{\left(\frac{3}{2}\right)}\left(\Omega_{\tau_p}, 0, 0\right) \hat{D}^{\left(\frac{3}{2}\right)}(0, \beta, 0) \\ &= d^{\left(\frac{3}{2}\right)}(-\beta) \text{diag}\left(e^{-i\frac{3}{2}\Omega_{Rabi}\tau_p}, e^{-i\frac{1}{2}\Omega_{Rabi}\tau_p}, e^{+i\frac{1}{2}\Omega_{Rabi}\tau_p}, e^{+i\frac{3}{2}\Omega_{Rabi}\tau_p}\right) d^{\left(\frac{3}{2}\right)}(\beta), \end{aligned} \quad (\text{B9})$$

where $d^{3/2}(\beta)$ is a Wigner small-d matrix for $j = 3/2$ and rotating angle β that is

$$d^{\left(\frac{3}{2}\right)}(\beta) \equiv \langle m' | e^{-i\beta \hat{S}_y} | m \rangle = \begin{pmatrix} c^3 & -\sqrt{3}c^2s & \sqrt{3}cs^2 & -s^3 \\ \sqrt{3}c^2s & c(c^2 - 2s^2) & (s^2 - 2c^2)s & \sqrt{3}cs^2 \\ \sqrt{3}cs^2 & (2c^2 - s^2)s & c(c^2 - 2s^2) & -\sqrt{3}c^2s \\ s^3 & \sqrt{3}cs^2 & \sqrt{3}c^2s & c^3 \end{pmatrix}. \quad (\text{B10})$$

where, $c \equiv \cos \frac{\beta}{2}$ and $s \equiv \sin \frac{\beta}{2}$. If $\delta \neq 0$ then $-\pi < \beta < 0$ and $c, s \neq 0$ with $1 - 2c^2 = \cos \beta \neq 0$. Hence, eq. B9 and B10 show that every \hat{U}_p element is a non-trivial linear combination of four complex phases $e^{-im\theta}$ with real weights so, generically, no structural zeros appear. To express the analytical form of the full 4×4 matrix of $\hat{U}_p(\tau_p)$, we additionally define new parameters, $\theta \equiv \Omega_{Rabi}\tau_p$, $q \equiv e^{-i\theta/2}$, $p \equiv e^{-3i\theta/2}$, then using eq. (B9) and (B10), we find the matrix elements of $\hat{U}_p(\tau_p)$ as below,

$$U_{-3/2, -3/2} = pc^6 + 3qc^4s^2 + 3q^*c^2s^4 + p^*s^6 = Z_1$$

$$U_{-3/2, -1/2} = \sqrt{3}cs[-pc^4 + qc^2(c^2 - 2s^2) + q^*s^2(2c^2 - s^2) + p^*s^4] = N_1$$

$$U_{-3/2, +1/2} = \sqrt{3}c^2s^2[pc^2 + q(s^2 - 2c^2) + q^*(c^2 - 2s^2) + s^2p^*] = D_1$$

$$U_{-3/2, +3/2} = c^3s^3(-p + 3q - 3q^* + p^*) = T_1$$

$$U_{-1/2, -1/2} = 3pc^4s^2 + qc^2(c^2 - 2s^2)^2 + q^*s^2(2c^2 - s^2)^2 + 3p^*c^2s^4 = Z_2$$

$$U_{-1/2, +1/2} = cs(c^2 - 2s^2)(2c^2 - s^2)(q^* - q) + 3c^3s^3(p^* - p) = N_2$$

$$U_{-1/2, +3/2} = \sqrt{3}c^2s^2[p^*c^2 + q^*(s^2 - 2c^2) + q(c^2 - 2s^2) + s^2p] = U_{13}^* = D_1^*$$

$$U_{+1/2, +1/2} = 3p^*c^4s^2 + q^*c^2(c^2 - 2s^2)^2 + qs^2(2c^2 - s^2)^2 + 3pc^2s^4 = U_{22}^* = Z_2^*$$

$$\begin{aligned}
U_{+1/2,+3/2} &= \sqrt{3}cs[p^*c^4 - q^*c^2(c^2 - 2s^2) - qs^2(2c^2 - s^2) - ps^4] = -U_{12}^* = -N_1^* \\
U_{+3/2,+3/2} &= p^*c^6 + 3q^*c^4s^2 + 3qc^2s^4 + ps^6 = U_{11}^* = Z_1^*
\end{aligned} \tag{B11}$$

We find that $U_p = U_p^T$ with anti-diagonal mirror-conjugation $U_{ij} = U_{-i,-j}^*$ and off-diagonal component symmetry as $U_{-1/2,-3/2} = U_{-3/2,-1/2}$, $U_{+1/2,-3/2} = U_{-3/2,+1/2}$, $U_{+3/2,-3/2} = U_{-3/2,+3/2}$, $U_{+1/2,-1/2} = U_{-1/2,+1/2}$, $U_{+3/2,-1/2} = U_{-1/2,+3/2}$, $U_{+3/2,+1/2} = U_{+1/2,+3/2}$. Also, $U_{+3/2,+3/2} = U_{-3/2,-3/2}^*$, $U_{+1/2,+1/2} = U_{-1/2,-1/2}^*$, $U_{-1/2,+3/2} = U_{-3/2,+1/2}^*$, and $U_{+1/2,+3/2} = -U_{-3/2,-1/2}^*$. $U_{+1/2,+3/2} = -U_{-3/2,-1/2}^*$.

Then, the observable becomes, according to eq. (B2),

$$S(\tau) = \langle \psi_f | \hat{O}_2 | \psi_f \rangle = c_0 + \sum_{m < n} 2|X_{mn}| \cos[\Omega_{mn}t - \arg X_{mn}], \tag{B12}$$

where

$$\begin{aligned}
c_0 &= U_{-3/2,-3/2}U_{-3/2,-1/2}U_{-3/2,-3/2}^*U_{-3/2,-1/2}^* + U_{-3/2,-1/2}U_{-1/2,-1/2}U_{-3/2,-1/2}^*U_{-1/2,-1/2}^* \\
&\quad + U_{-3/2,+1/2}U_{+1/2,-1/2}U_{-3/2,+1/2}^*U_{+1/2,-1/2}^* + U_{-3/2,+3/2}U_{+3/2,-1/2}U_{-3/2,+3/2}^*U_{+3/2,-1/2}^* \\
X_{-3/2,-1/2} &= U_{-3/2,-1/2}U_{-1/2,-1/2}^*(U_{-3/2,-3/2}U_{-3/2,-1/2}^* + U_{+3/2,-3/2}U_{+3/2,-1/2}^*) \\
X_{-3/2,+1/2} &= U_{-3/2,-1/2}U_{+1/2,-1/2}^*(U_{-3/2,-3/2}U_{-3/2,+1/2}^* + U_{+3/2,-3/2}U_{+3/2,+1/2}^*) \\
X_{-3/2,+3/2} &= U_{-3/2,-1/2}U_{+3/2,-1/2}^*(U_{-3/2,-3/2}U_{-3/2,+3/2}^* + U_{+3/2,-3/2}U_{+3/2,+3/2}^*) \\
X_{-1/2,+1/2} &= U_{-1/2,-1/2}U_{+1/2,-1/2}^*(U_{-3/2,-1/2}U_{-3/2,+1/2}^* + U_{+3/2,-1/2}U_{+3/2,+1/2}^*) \\
X_{-1/2,+3/2} &= U_{-1/2,-1/2}U_{+3/2,-1/2}^*(U_{-3/2,-1/2}U_{-3/2,+3/2}^* + U_{+3/2,-1/2}U_{+3/2,+3/2}^*) \\
X_{+1/2,+3/2} &= U_{+1/2,-1/2}U_{+3/2,-1/2}^*(U_{-3/2,+1/2}U_{-3/2,+3/2}^* + U_{+3/2,+1/2}U_{+3/2,+3/2}^*).
\end{aligned} \tag{B13}$$

At this point, the main objective of Appendix B is achieved by finding the cosine term in Eq. (B12). Because the final $\pi/2$ pulse is a generic unitary acting on the four-level manifold, its matrix elements are in general nonzero, and multiplying U_p by the freely evolving state inevitably mixes the pairwise phases accumulated between all sublevel pairs. Consequently, the measured signal can always be organized as a sum of cosine terms oscillating at the six pairwise splittings Ω_{mn} . Finding the explicit form of the coefficient of each cosine term, X_{mn} is not strictly required for establishing the frequency set; they are included to show explicitly that the second $\pi/2$ pulse is nontrivial and to obtain a closed-form expression under the hard-pulse approximation. However, this approximation also introduces an unavoidable inconsistency in the weights X_{mn} . A representative example is the

$(m, n) = (-1/2, +1/2)$ contribution associated with the $| -1/2 \rangle \leftrightarrow | +1/2 \rangle$ pair, whose oscillation frequency is $\Omega_{23} = \delta + 2D_{gs}$: within the hard-pulse model, the corresponding coefficient collapses algebraically to $X_{23} = 0$, whereas the full numerical propagation used in the main text (Fig. 2 and 4(a)) shows that this component can be one of the strongest. We therefore attribute this discrepancy to the limitations of the hard-pulse approximation in our regime, where ω_1 is not asymptotically larger than the relevant splittings (D_{gs} and δ), and stress that Eqs. (B5)–(B13) should be interpreted as a constructive demonstration of the six-frequency cosine decomposition in Eq. (B12), not as a quantitatively accurate prediction of all branch weights under experimental conditions.

References

- [1] R. Z. Fang *et al.*, Experimental Generation of Spin-Photon Entanglement in Silicon Carbide, *Physical Review Letters* **132** (2024).
- [2] C. Babin *et al.*, Fabrication and nanophotonic waveguide integration of silicon carbide colour centres with preserved spin-optical coherence, *Nature Materials* **21**, 67 (2022).
- [3] T. Steidl *et al.*, Single V2 defect in 4H silicon carbide Schottky diode at low temperature, *Nature Communications* **16** (2025).
- [4] C. P. Anderson *et al.*, Electrical and optical control of single spins integrated in scalable semiconductor devices, *Science* **366**, 1225 (2019).
- [5] B. P. Cyrus Zeledon, Jonathan C. Marcks, Mykyta Onizhuk, Yeghishe Tsaturyan, Yu-xin Wang, Benjamin S. Soloway, Hiroshi Abe, Misagh Ghezellou, Jawad Ul-Hassan, Takeshi Ohshima, Nguyen T. Son, F. Joseph Heremans, Giulia Galli, Christopher P. Anderson, David D. Awschalom, Minute-long quantum coherence enabled by electrical depletion of magnetic noise, *arXiv:2504.13164* (2025).
- [6] D. M. Lukin *et al.*, 4H-silicon-carbide-on-insulator for integrated quantum and nonlinear photonics, *Nat Photonics* **14**, 330 (2020).
- [7] R. Nagy *et al.*, Quantum Properties of Dichroic Silicon Vacancies in Silicon Carbide, *Phys Rev Appl* **9** (2018).
- [8] H. B. Banks, Ö. O. Soykal, R. L. Myers-Ward, D. K. Gaskill, T. L. Reinecke, and S. G. Carter, Resonant Optical Spin Initialization and Readout of Single Silicon Vacancies in 4H-SiC, *Phys Rev Appl* **11** (2019).
- [9] M. Niethammer, M. Widmann, S. Y. Lee, P. Stenberg, O. Kordina, T. Ohshima, T. Son, E. Janzén, and J. Wrachtrup, Vector Magnetometry Using Silicon Vacancies in 4H-SiC Under Ambient Conditions, *Phys Rev Appl* **6** (2016).

[10] E. Sörman, N. T. Son, W. M. Chen, O. Kordina, C. Hallin, and E. Janzén, Silicon vacancy related defect in 4H and 6H SiC, *Phys Rev B* **61**, 2613 (2000).

[11] P. Udvarhelyi *et al.*, Vibronic States and Their Effect on the Temperature and Strain Dependence of Silicon-Vacancy Qubits in 4H-SiC, *Phys Rev Appl* **13** (2020).

[12] R. Nagy *et al.*, High-fidelity spin and optical control of single silicon-vacancy centres in silicon carbide, *Nature Communications* **10**, 1954 (2019).

[13] M. Widmann *et al.*, Coherent control of single spins in silicon carbide at room temperature, *Nature Materials* **14**, 164 (2015).

[14] E. Hesselmeier *et al.*, Qudit-Based Spectroscopy for Measurement and Control of Nuclear-Spin Qubits in Silicon Carbide, *Physical Review Letters* **132** (2024).

[15] P. J. Low, B. White, and C. Senko, Control and readout of a 13-level trapped ion qudit, *Npj Quantum Information* **11** (2025).

[16] P. Hrmo, B. Wilhelm, L. Gerster, M. W. van Mourik, M. Huber, R. Blatt, P. Schindler, T. Monz, and M. Ringbauer, Native qudit entanglement in a trapped ion quantum processor, *Nature Communications* **14** (2023).

[17] T. C. Ralph, K. J. Resch, and A. Gilchrist, Efficient Toffoli gates using qudits, *Phys Rev A* **75** (2007).

[18] B. L. Brock, S. Singh, A. Eickbusch, V. V. Sivak, A. Z. Ding, L. Frunzio, S. M. Girvin, and M. H. Devoret, Quantum error correction of qudits beyond break-even, *Nature* **641** (2025).

[19] N. V. V. Branislav Ilikj, Ramsey Interferometry with Qudits, *arXiv:2509.06290* (2025).

[20] M. Malinowski *et al.*, Generation of a Maximally Entangled State Using Collective Optical Pumping, *Physical Review Letters* **128** (2022).

[21] F. Motzoi, J. M. Gambetta, P. Rebentrost, and F. K. Wilhelm, Simple Pulses for Elimination of Leakage in Weakly Nonlinear Qubits, *Physical Review Letters* **103**, 110501 (2009).

[22] M. Sarovar, T. Proctor, K. Rudinger, K. Young, E. Nielsen, and R. Blume-Kohout, Detecting crosstalk errors in quantum information processors, *Quantum* **4** (2020).

[23] M. J. Peterer *et al.*, Coherence and Decay of Higher Energy Levels of a Superconducting Transmon Qubit, *Physical Review Letters* **114** (2015).

[24] I. M. Georgescu, S. Ashhab, and F. Nori, Quantum simulation, *Rev Mod Phys* **86**, 153 (2014).

[25] M. Saffman, T. G. Walker, and K. Mølmer, Quantum information with Rydberg atoms, *Rev Mod Phys* **82**, 2313 (2010).

[26] M. W. Doherty, N. B. Manson, P. Delaney, F. Jelezko, J. Wrachtrup, and L. C. L. Hollenberg, The nitrogen-vacancy colour centre in diamond, *Phys Rep* **528**, 1 (2013).

[27] Z. Chen *et al.*, Measuring and Suppressing Quantum State Leakage in a Superconducting Qubit, Physical Review Letters **116**, 020501 (2016).

[28] S. T. Merkel, J. M. Gambetta, J. A. Smolin, S. Poletto, A. D. Córcoles, B. R. Johnson, C. A. Ryan, and M. Steffen, Self-consistent quantum process tomography, Phys Rev A **87** (2013).

[29] G. D. Fuchs, A. L. Falk, V. V. Dobrovitski, and D. D. Awschalom, Spin Coherence during Optical Excitation of a Single Nitrogen-Vacancy Center in Diamond, Physical Review Letters **108** (2012).

[30] B. Chen, J. P. Geng, F. F. Zhou, L. L. Song, H. Shen, and N. Y. Xu, Quantum state tomography of a single electron spin in diamond with Wigner function reconstruction, Appl Phys Lett **114** (2019).

[31] L. G. Lutterbach and L. Davidovich, Method for direct measurement of the Wigner function in cavity QED and ion traps, Physical Review Letters **78**, 2547 (1997).

[32] S. Deléglise, I. Dotsenko, C. Sayrin, J. Bernu, M. Brune, J. M. Raimond, and S. Haroche, Reconstruction of non-classical cavity field states with snapshots of their decoherence, Nature **455**, 510 (2008).

[33] S. Y. Lee, M. Niethammer, and J. Wrachtrup, Vector magnetometry based on S=3/2 electronic spins, Phys Rev B **92** (2015).

[34] M. H. Levitt, *Spin dynamics : basics of nuclear magnetic resonance* (John Wiley & Sons, Chichester, England ; Hoboken, NJ, 2008), 2nd edn.

[35] C. P. Slichter, *Principles of magnetic resonance* (Springer-Verlag, Berlin ; New York, 1992), 3rd enl. and updated edn., Springer series in solid-state sciences, 1.

[36] N. F. Ramsey, A Molecular Beam Resonance Method with Separated Oscillating Fields, Physical Review **78**, 695 (1950).

[37] C. L. Degen, F. Reinhard, and P. Cappellaro, Quantum sensing, Rev Mod Phys **89** (2017).

[38] J. Park, S. Paik, S. J. Hwang, D. Liu, Ö. O. Soykal, J. Wrachtrup, and S. Y. Lee, Mechanism for selective initialization of silicon-vacancy spin qubits with S=3/2 in silicon carbide, Phys Rev Appl **21** (2024).

[39] N. Morioka *et al.*, Spin-Optical Dynamics and Quantum Efficiency of a Single V1 Center in Silicon Carbide, Physical Review Applied **17** (2022).

[40] D. Liu *et al.*, The silicon vacancy centers in SiC: determination of intrinsic spin dynamics for integrated quantum photonics, Npj Quantum Information **10** (2024).

[41] P. Udvarhelyi, R. Nagy, F. Kaiser, S. Y. Lee, J. Wrachtrup, and A. Gali, Spectrally Stable Defect Qubits with no Inversion Symmetry for Robust Spin-To-Photon Interface, Phys Rev Appl **11** (2019).

[42] W. Z. Dong, M. W. Doherty, and S. E. Economou, Spin polarization through intersystem crossing in the silicon vacancy of silicon carbide, Phys Rev B **99** (2019).

- [43] C. Bengs and M. H. Levitt, SpinDynamica: Symbolic and numerical magnetic resonance in a Mathematica environment, *Magnetic Resonance in Chemistry* **56**, 374 (2018).
- [44] C. E. Shannon, Communication in the presence of noise (Reprinted from the Proceedings of the IRE, vol 37, pg 10-21, 1949), *P IEEE* **86**, 447 (1998).
- [45] M. Unser, Sampling - 50 years after Shannon, *P IEEE* **88**, 569 (2000).
- [46] J. J. Sakurai and J. Napolitano, *Modern Quantum Mechanics* (Cambridge University Press, 2020).